Contact NOC NORA team at
publications@noc.soton.ac.uk

Shear at the Base of the Oceanic Mixed Layer Generated by Wind Shear Alignment

LIAM BRANNIGAN

School of Ocean Sciences, Bangor University, Menai Bridge, Wales, and Atmospheric, Oceanic and Planetary Physics, University of Oxford, Oxford, United Kingdom

YUENG-DJERN LENN AND TOM P. RIPPETH

School of Ocean Sciences, Bangor University, Menai Bridge, Wales, United Kingdom

ELAINE MCDONAGH

National Oceanography Centre, Southampton, United Kingdom

TERESA K. CHERESKIN AND JANET SPRINTALL

Scripps Institution of Oceanography, University of California, San Diego, La Jolla, California

ABSTRACT

Observations are used to evaluate a simple theoretical model for the generation of near-inertial shear spikes at the base of the open ocean mixed layer when the upper ocean displays a two-layer structure. The model predicts that large changes in shear squared can be produced by the alignment of the wind and shear vectors. A climatology of stratification and shear variance in Drake Passage is presented, which shows that these assumptions are most applicable to summer, fall, and spring but are not highly applicable to winter. Temperature, salinity, and velocity data from a high spatial resolution cruise in Drake Passage show that the model does not predict all large changes in shear variance; the model is most effective at predicting changes in shear squared when it arises owing to near-inertial wind-driven currents without requiring a rotating resonant wind stress. The model is also more effective where there is a uniform mixed layer above a strongly stratified transition layer. Rotary spectral and statistical analysis of an additional 242 Drake Passage transects from 1999 to 2011 confirmed the presence of this shear-spiking mechanism, particularly in summer, spring, and fall when stratification is stronger.

1. Introduction

The surface layer of the ocean is a major component of the planetary boundary layer. Processes within the surface mixed layer determine the size and direction of momentum, heat, and tracer fluxes between the atmosphere and the ocean interior and so have implications for the planetary climate and its variability (Sullivan and McWilliams 2010). These fluxes also play an important role in linking the oceanic and atmospheric carbon pools through regulation of the sea surface CO_2 fluxes (Mahadevan et al. 2012).

The wind stress on the ocean surface is the direct energy source for many types of fluid motion in the ocean. It is known to generate flows that range from basin-scale (e.g., Marshall and Pillar 2011) to much smaller–scale flows such as Langmuir circulation (Thorpe 2004). A number of pathways to dissipation exist for energy derived from the wind stress in the surface ocean, though their relative importance is poorly understood (Johnston and Rudnick 2009). These include surface wave generation, Langmuir turbulence (Polton et al. 2008), and inertial oscillations (Pollard and Millard 1970). The impact of these processes is largely confined to the surface mixed layer. Below this a highly stratified transition layer inhibits the downward transfer of momentum (Grant and Belcher 2011) and, thus, gives rise to a maximum shear layer widely observed in the global ocean (Johnston and Rudnick 2009). Nonetheless, some

of the energy associated with the Langmuir turbulence and near-inertial oscillations is also thought to generate internal waves that then propagate into the ocean interior (e.g., Polton et al. 2008; Dohan and Davis 2011).

Although the time-average shear in the transition layer is generally higher than at other depths, it is also the layer of strongest stratification, and consequently the water column is often at near-critical stability (Richardson number ≈ 1; Johnston and Rudnick 2009). The low Richardson number implies that periods of enhanced shear may induce instabilities, leading to water column mixing and the dissipation of turbulent kinetic energy. D'Asaro (1985) noted that an alignment of the wind and surface current can give rise to such an increase in shear while Rippeth et al. (2009) observed an enhancement in shear associated with wind shear alignment that resulted in a tripling of the observed turbulent dissipation rate in the seasonal thermocline of a temperate shelf sea. Burchard and Rippeth (2009, hereafter BR09) derived a prognostic expression for shear variance in a shallow, stratified tidal sea from a simplified set of the equations of motion. The model demonstrated that the alignment of the wind and shear can lead to a sharp increase in shear variance over a period of hours or less (and so has been termed a shear spike).

Observations from other stratified shelf sea locations, in the northern North Sea (BR09) and the ice-covered Laptev Sea (Lenn et al. 2011), show the coincidence of enhanced dissipation within the thermocline and an increase in shear resulting from the alignment of the shear vector with the surface wind stress. The observations made in the Irish Sea and North Sea had similar levels of wind forcing $[O(10^{-1}\,\mathrm{N\,m^{-2}})]$ and stratification $[O(10^{-4}\,\mathrm{s^{-2}})]$ to that found in open ocean conditions, suggesting that it may be possible to modify the BR09 model for the open ocean. While much attention has focused on resonant wind-driven mixing at the base of the mixed layer (e.g., D'Asaro 1985; Skyllingstad et al. 1998; Grant and Belcher 2011; Dohan and Davis 2011) these spikes in dissipation occurred without resonant wind forcing, suggesting that they may be a ubiquitous feature of the seasonal thermocline.

In this study, we use data from the Southern Ocean mixed layer and seasonal thermocline to confirm the existence of nonresonant shear spikes in the open ocean. The primary aims of the paper are to modify BR09 for the open ocean surface boundary layer, test the validity of the assumptions underlying the model, and assess its skill in predicting the generation of shear spikes.

The data consist of a slow transect (11 days) of the Drake Passage region made by the RRS *James Cook* (hereafter *Cook*) in February 2009 and 242 faster transects (2–5 days) of Drake Passage made by the ARSV

Laurence M. Gould (*LMG*) between 1999 and 2011 (Fig. 1a). An analytical model for the production of shear squared (i.e., S^2) in an open ocean environment is derived in section 2. The datasets and methods employed are then described in section 3. The overall structure of the stratification and shear are set out in section 4. The effectiveness of the model is evaluated in section 5 with a summary and discussion following in section 6.

2. Shear production model

The central idea of the model is that interaction between shear and local wind forcing is an important source for the production or dissipation of shear variance and that an expression for this can be derived from a simplified set of the equations of motion. The model provides a prognostic equation for changes in shear variance that can be tested by comparison with observations. The validity of these assumptions is tested against the observations in sections 4 and 5.

In the model, the assumption has been made that dynamically important shear can be represented by a two-layer damped-slab model with an upper layer subject to wind forcing. Both of the layers are subject to an interfacial friction that acts to smooth velocity gradients between the layers. This interfacial friction is intended to parameterize relatively laminar vertical momentum fluxes rather than the much larger fluxes that arise when shear instabilities develop, as the model is intended to predict the generation of such instabilities rather than describe their subsequent effects.

BR09 based their continental shelf sea model for shear production on a one-dimensional momentum balance between linear and Coriolis acceleration, the surface wind and bottom tidal stresses, and interfacial friction. For the surface open ocean where vertical velocity gradients due to tides are weak, we can express the vertically-averaged momentum balance, following Pollard and Millard (1970), in the respective layers as

$$\frac{\partial \mathbf{u}_s}{\partial t} + f\mathbf{k} \times \mathbf{u}_s = \frac{\boldsymbol{\tau}_w - \boldsymbol{\tau}_i}{\rho H} \quad \text{and} \quad (1\mathrm{a})$$

$$\frac{\partial \mathbf{u}_l}{\partial t} + f\mathbf{k} \times \mathbf{u}_l = \frac{\boldsymbol{\tau}_i}{\rho H}, \quad (1\mathrm{b})$$

where the surface and lower layers are indicated by the subscripts s and l, $\mathbf{u}$ is the horizontal velocity vector, $\mathbf{k}$ is the vertical unit vector, t is time, $\partial/\partial t$ is the time derivative, f is the Coriolis parameter, ρ is potential density, $\boldsymbol{\tau}_w$ is the relative wind stress vector, $\boldsymbol{\tau}_i$ is the interfacial frictional stress vector, and H is the mixed layer depth (MLD). Note that surface stress is taken to
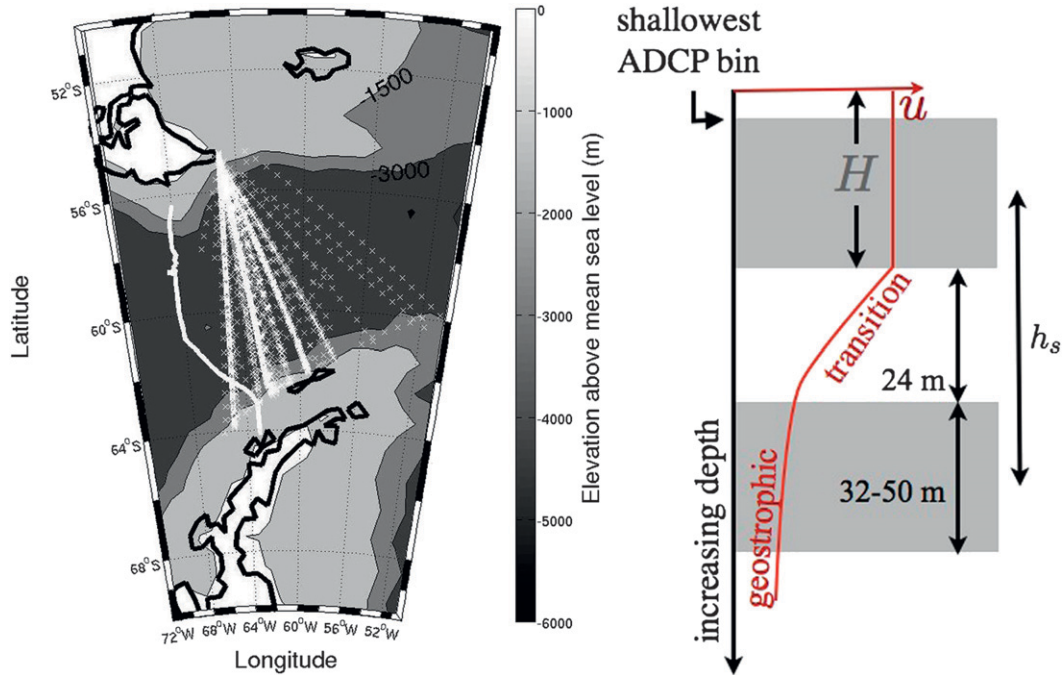
FIG. 1. (a) Map of Drake Passage with bathymetry in grayscale and contour lines at 1500 m, 3000 m, and 4500 m. The solid line shows the track of the high-resolution *James Cook* transect, while the crosses mark the *Laurence M. Gould* crossings. (b) A schematic of the vertical structure used to calculate the bulk shear. The gray-shaded areas represent the layers over which velocity is averaged, H is the mixed layer depth, and h_s is the distance between the centers of mass of the upper and lower layers.

be the relative wind stress, calculated from the velocity of the wind relative to the surface ocean current. Hereafter, the body forces owing to wind and interfacial friction are denoted as $\mathbf{T}_w$ and $\mathbf{T}_i$, respectively, which are the stresses divided by ρ (making the assumption that spatial and temporal variations in ρ are much smaller than its mean value, so it can be taken as a constant).

The damped-slab mixed layer model assumes that diffusion of momentum is rapid within each layer, such that the divergence of the wind and interfacial boundary stresses can be treated as body forces applied equally over the whole layer. The nonlinear advective term between layers in the absence of shear instability is thought to be weak (Polton et al. 2008) and so is neglected. As we are only concerned with the mechanism responsible for the generation of shear spikes, we assume there to be no shear instability, although in consideration of mixing we note the shear instability will actually be the dominant process for the dissipation of kinetic energy (Plueddemann and Farrar 2006). As such, the model understates the destruction of S^2 after shear spikes where this is brought about by instabilities. Finally, the vertical pressure gradient term is excluded as an implicit assumption that the water column is statically stable has been made. The role of horizontal pressure and velocity gradients is a subject of on-going research.

The momentum balance of (1) can be adapted into shear form. The relationship between velocity and bulk shear is as follows:

$$\mathbf{S} = \frac{\mathbf{u}_s - \mathbf{u}_l}{h_s}, \tag{2}$$

where h_s is the distance between the centers of mass of the upper layer (above the mixed layer base) and lower layer (below the mixed layer base), which is assumed to be constant in time. Following the approach of BR09, we can substitute (2) into (1) by subtracting (1b) from (1a) and dividing all terms by h_s, giving

$$\frac{\partial \mathbf{S}}{\partial t} + f\mathbf{k} \times \mathbf{S} = \frac{\mathbf{T}_w - \mathbf{T}_i}{h_s H}. \tag{3a}$$

We then take the dot product of this equation with $\mathbf{S}$ to obtain an equation for shear variance:

$$\frac{1}{2}\frac{\partial S^2}{\partial t} + \mathbf{S} \cdot (f\mathbf{k} \times \mathbf{S}) = \mathbf{S} \cdot \left(\frac{\mathbf{T}_w - \mathbf{T}_i}{h_s H}\right), \tag{4}$$

where the second term on the left-hand side is zero (as it represents the Coriolis force rotating shear without changing its variance). Rearranging (4) then gives

$$\frac{\partial S^2}{\partial t} = 2\left(\frac{\mathbf{S}}{h_s} \cdot \frac{\mathbf{T}_w}{H} - \frac{\mathbf{S}}{h_s} \cdot \frac{\mathbf{T}_i}{H}\right) \qquad (5)$$

or

$$\frac{\partial S^2}{\partial t} = P(S^2) - D(S^2), \qquad (6)$$

where $P(S^2)$ denotes the production/destruction of S^2 (dependent on the relative alignment of the wind and shear vectors) and $D(S^2)$ denotes the negative-definite destruction of S^2 by interfacial friction.

Finally, the interfacial friction body force $\mathbf{T}_i$ can be parameterized using a quadratic friction law (following BR09) as

$$\mathbf{T}_i = c_i(\mathbf{u}_s - \mathbf{u}_l)|\mathbf{u}_s - \mathbf{u}_l| = c_i h_s^2 \mathbf{S}|\mathbf{S}|, \qquad (7)$$

where c_i is the drag coefficient. This allows (5) to be restated as

$$\frac{\partial S^2}{\partial t} = 2\left(\frac{\mathbf{S}}{h_s} \cdot \frac{\mathbf{T}_w}{H} - c_i \frac{h_s}{H}|S^3|\right). \qquad (8)$$

This simple theoretical model predicts that alignment of wind and shear produces the maximum value for the production of S^2. Note, however, that, if the shear vector is rotating, S^2 continues to increase after the point of alignment and only reaches its maximum value where (5) is zero, that is, when wind and shear are 90° out of phase.

The model addresses changes in S^2 at time scales of hours or less, over which time scales the MLD generally varies much less than the other terms and so is held constant in the model. However, the variations in MLD at monthly time scales are comparable to the variations in the other factors and so are considered in the observations of the annual cycle in section 4a. The effectiveness of the model is considered further in section 5.

3. Data and methods

a. Datasets

Two Drake Passage datasets are used for this analysis. The densely sampled hydrographic survey from the *Cook* provides a long (11 day) pseudo time series used to evaluate the model for specific conditions over a transect that lasted 19 inertial periods. The comparatively fast (~2 day) repeat transects spanning the 12 years of the *LMG* dataset are used to evaluate the model over transects typically lasting fewer inertial periods (typically 5–6) but covering the full range of conditions experienced through the annual cycle. As the focus here is

on open ocean processes, data gathered from continental shelf and slope areas (i.e., bathymetry <1500-m depth) are excluded from the analysis. Drake Passage sections encompass only two wind decorrelation length scales (≈500 km, Gille 2005), so it is reasonable to treat each transect as a virtual time series, and two degrees of freedom are assumed when conducting spectral analysis across a whole transect.

The *Cook* observations are from a hydrographic survey of Drake Passage gathered on the JC31 cruise in February 2009 (Hamersley and McDonagh 2009) from South America toward the West Antarctic Peninsula (Fig. 1a). This was a dedicated oceanographic cruise with frequent stops to perform full-depth hydrographic casts with a conductivity–temperature–depth (CTD) instrument and both lowered- and ship-mounted acoustic Doppler current profilers (ADCP). It took place from 3 February to 3 March 2009 in the late austral summer. This included a further survey northbound from the West Antarctic Peninsula toward the Falkland Islands. This second survey did not display a strong inertial signal, presumably due to aliasing by spatial features such as eddies, and so is not included in the analysis here.

The *LMG* dataset consists of underway observations from 242 crossings of Drake Passage made between 1999 and 2011. The *LMG* transects lay primarily to the east of the *Cook* survey and fan out from Cape Horn toward the south, with some clustering along the directly southbound transect at the western end of the domain (Fig. 1a). Upper-ocean currents were measured by the *LMG* ship-mounted ADCP during year-round crossings of the Passage as part of regular resupply trips to Palmer Station on Anvers Island off the West Antarctic Peninsula or for specialist scientific cruises in the region. The hydrographic data came from the deployment of expendable bathythermograph (XBT) and expendable conductivity–temperature–depth (XCTD) probes. The 242 *LMG* ADCP surveys used in this study were conducted between September 1999 and April 2011, while the 96 XBT/XCTD surveys were conducted between September 1996 and February 2011. There are ADCP and XBT/XCTD data from all months but with fewer transects in July and August.

The velocity data used in this study were sampled using 153.6 kHz RDI ADCPs. On the *Cook*, the ADCP was mounted on the portside retractable drop keel. When the keel was extended, transducer depth was approximately 9.6 m and only these data are used here. The *LMG* ADCP is located in a special antifreeze-filled sonar pod that sits below bubbles in order to minimize data noise in the surface boundary layer (Firing et al. 2012). The speed of sound through the antifreeze is measured independently, and the ADCP data were adjusted accordingly [see Lenn et al. (2007) for further details]. Both *Cook* and *LMG*

ADCP data were collected with a vertical bin length of 8 m with a first depth of 23.5 m for the *Cook* data and 26 m for the *LMG* data. The temporal averaging was 5-min ensembles for the *Cook* dataset and 15-min ensembles for the much larger *LMG* dataset.

During the *Cook* transect, 47 full-depth CTD profiles were collected, typically at separations of 30 km. The instrument used was a Seabird 911plus with a 300-kHz RDI Workhorse ADCP unit attached to the rosette with an altimeter pinger to ascertain the bottom depth at the point of each CTD deployment (used to determine where the bathymetry criterion of depth greater than 1500 m was met). The *LMG* hydrographic profiles were made using Sippican Deep Blue XBT and TSK Digital XCTD probes. The XBTs record temperature data with 2-m vertical resolution and were deployed with 6–15 km along-track resolution. These observations were objectively mapped (Roemmich 1983) to a grid with 10-m vertical resolution and 0.1° latitudinal resolution. A decorrelation scale of 40 km and an error variance of 0.1 were chosen so that estimates near the gridded data points closely match the observations. Since 2001 XCTDs deployed in Drake Passage have also recorded both temperature and salinity data with a vertical resolution finer than 1 m. The XCTDs have been deployed more sparsely than the XBTs with an along-track resolution of 25–100 km. Salinity is inferred from historical climatology using a position-dependent T–S–z relation, which is adjusted for salinity anomalies observed by the XCTDs when available [see Sprintall (2003) for more details]. The adjusted salinities were objectively mapped to the same 10-m vertical resolution and 0.1° latitudinal resolution as the XBT data. Density was then calculated using the objectively mapped temperature and salinity fields.

Wind data were recorded by onboard meteorological data systems and averaged into one-minute ensembles. *Cook* wind speed and direction were recorded by a Gill Windsonic anemometer located on a foremast at a height 16 m above the waterline, while *LMG* wind speed and direction were recorded by port and starboard RM Young 5106 anemometers located on the ship's main mast at a height 30 m above the waterline. This system became available in September 2000 giving 210 transects with ADCP and wind data.

b. Methods

The buoyancy frequency squared (i.e., N^2) was calculated as

$$N^2 = -\frac{g}{\rho_0}\frac{\partial\rho}{\partial z}, \qquad (9)$$

where g is gravitational acceleration, ρ is the potential density, z is the depth, and ρ_0 is a reference potential density.

The MLD was defined for the *Cook* data [following the definition of the Dong et al. (2008) Southern Ocean MLD climatology] as the shallowest depth where the potential density was 0.03 kg m^{-3} greater than at the surface. The upper layer, defined for the *Cook* bulk shear, extended from the ADCP depth bin centered at 31.5-m depth (having excluded the shallowest layer centered at 23.5 m due to occasional missing observations) to the depth closest to the MLD. The mean MLD on the *Cook* transect was 50 m, so the mixed layer velocity was typically the average of three ADCP depth bins. A gap of 24 m—which accounts for the portion of the water column with the highest gradients—is left between the upper layer and the lower layer. The lower layer is taken to be 32 m thick to give a representative velocity with reduced instrument noise. The size of the gap is based on a conservative estimate for the thickness of the high shear transition layer from Johnston and Rudnick (2009). The MLD for the *LMG* bulk shear layers were given by the Dong et al. (2008) climatology. The *LMG* upper layer extended from the first gridded depth at 26 m to the depth closest to the MLD. The *LMG* lower layer was up to 50 m thick where the data were available, with a 24 m gap between the two layers. The bulk shear is then the difference between the layer-averaged velocities divided by the distance between their centers of mass. A schematic illustrating the vertical structure of the bulk shear calculation is shown in Fig. 1b. A comparison of the bulk shear and the shear taken between successive ADCP depth bins for the *Cook* transect (not shown) confirms that the bulk shear has less high frequency variability than the interfacial shear but generally captures the variability in the interfacial shear at periods longer than a few hours.

The bulk shear time series are presented without interpolation, with details of any filters used noted in the relevant figure captions. When the bulk shear is used in Fourier spectral analysis, linear interpolation within transects is used to fill in missing data. When the *LMG* data are used, the Fourier components are computed transect by transect and then averaged to produce the spectra, with each transect providing two degrees of freedom. The separation of the data into transects acts as a natural windowing operation, so no further filters have been applied. The *LMG* ADCP data are also used to estimate a monthly latitude–depth climatology of shear in Drake Passage in section 4a. For this calculation, the shear for each 15-min-averaged velocity profile is estimated as the vertical centered difference of velocity with depth. The shear profiles for each transect are averaged in 0.1° latitude bins, and the transects are then averaged together by month.
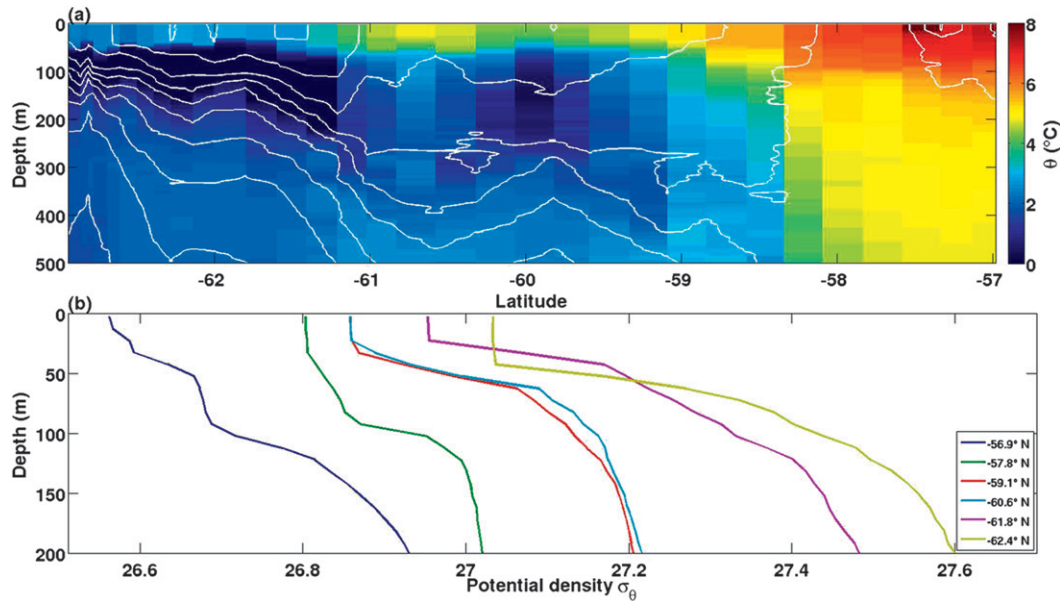
FIG. 2. Hydrographic profiles of the *James Cook* transect. (a) The potential temperature profiles with 0.1 psu salinity contours overlain showing the contrast between the thermally stratified region in the north of Drake Passage and the salinity stratified region in the south. (b) Potential density profiles from a selection of individual CTD casts show that the mixed layers were more sharply defined in the south of the Passage than the north.

The wind data are used to estimate the 10-m wind components using the boundary layer profile of Large and Pond (1981). The relative wind speed was calculated by subtracting the surface ocean current (using the shallowest ADCP depth bins as a proxy) from the calculated 10-m wind before using the Large and Pond (1981) parameterization to calculate the relative wind stress. This parameterization assumes that the atmosphere is of neutral stability, and the air density was taken as $1.25 \, \mathrm{kg \, m^{-3}}$ throughout. Large and Pond (1981) note that there is an error in the calculated stress of less than 10% in converting the wind speed from the observed wind to the 10-m wind and this error decreases with wind speed. If the magnitude of the atmospheric stability parameter (the Monin–Obukhov length) is on the order of the observation height this can introduce a further 20% error in the calculated stress. We assume, however, that these errors are bounded in the evaluation of the model as stronger winds tend to induce neutral stability in the atmospheric boundary layer and, furthermore, these errors do not affect the direction of the wind stress, which is the most critical part of our analysis. For the *Cook* dataset there were no observations of wind speed greater than the $25 \, \mathrm{m \, s^{-1}}$ upper limit, and only 0.7% of the observations in the *LMG* dataset exceeded this limit.

Data are analyzed by season to observe temporal patterns. Here austral summer is taken to be January–March, austral fall is April–June, austral winter is July–September, and austral spring is October–December.

4. Characteristics of stratification and shear

The model set out in section 2 assumes the upper ocean has a two-layer structure that surrounds a stratified transition layer where shear is concentrated. In this section, we describe the seasonal variability of Drake Passage upper-ocean shear and stratification to test this assumption and investigate the statistical and rotary properties of bulk shear.

a. Annual cycle

The temperature and salinity profiles from the *Cook* transect in Fig. 2a provide a snapshot of Drake Passage hydrography. It shows that in the north of Drake Passage the surface layer was not homogeneous but, instead, had a weak thermal stratification (Figs. 2a,b). In the south of Drake Passage there was a thermal inversion with static stability maintained by strong haline stratification (Fig. 2a). However, this region had a uniform mixed layer at the surface above a sharp transition layer (Fig. 2b).

Seasonal variability in the vertical water column structure characterizes the calculated *LMG* monthly mean N^2 sections (Fig. 3). Beginning in the austral spring (October–November in Fig. 3), surface layer stratification develops above 150-m depth. This intensifies and shoals throughout
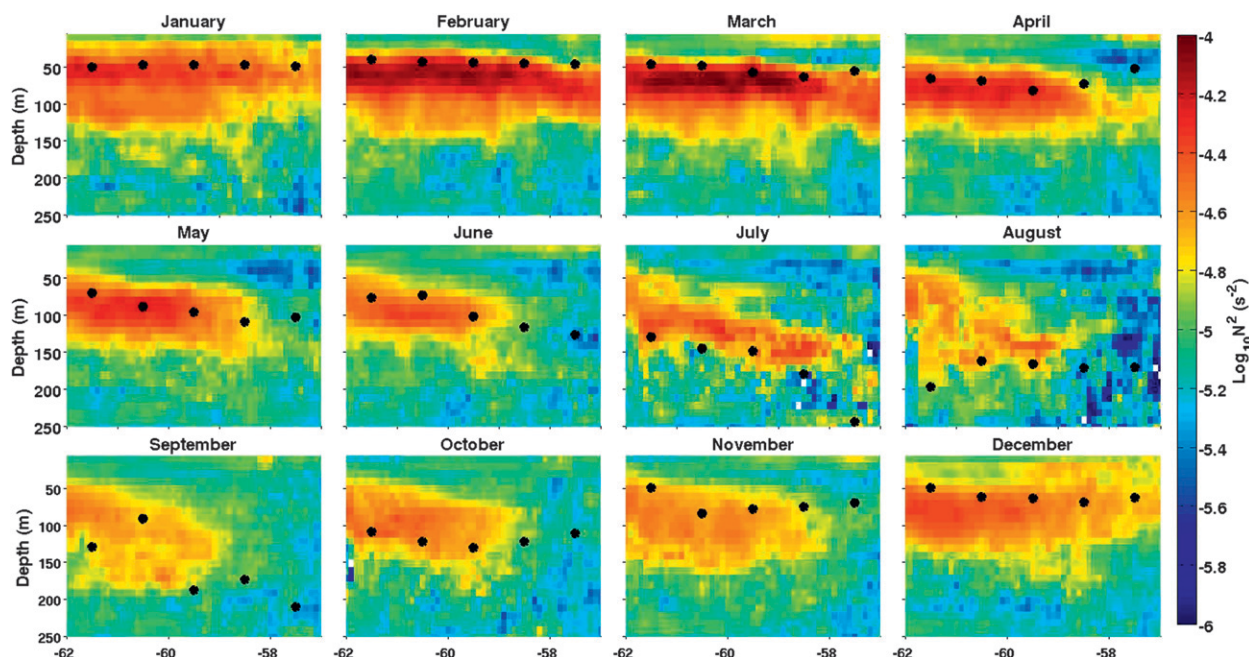
FIG. 3. Estimation of $\log_{10}N^2$ in Drake Passage for the *Laurence M. Gould* transects based on a 0.1° objective mapping of temperature and salinity: N^2 is observed for each transect separately and then averaged by month; values of N^2 less than zero in any profile are excluded. The Dong et al. (2008) mixed layer depth climatology is marked by black dots.

the austral summer and peaks in March when the MLD is at ~40 m depth. As fall sets in, this stratification weakens and is substantially eroded by late winter (August in Fig. 3). In addition, there is a clear tendency for stratification to be stronger in the south of the passage throughout the year (Fig. 3). Note that at the southern end of the latitude range the tracks are relatively spaced out (Fig. 1a), so an assumption has been made that the primary gradients are meridional to perform this analysis of the monthly data.

The effect of the seasonal cycle on shear variance is apparent from Fig. 4. From October into the austral summer (Fig. 4) the peak shear variance increases and the depth of the shear maximum shoals, being shallowest in February–April. After May the shear variance weakens by about an order of magnitude while the depth of the shear maximum also deepens. An analysis of shear variance over the upper 1000 m in Drake Passage by Firing et al. (2011) demonstrated that this is, indeed, the portion of the water column with the highest shear variance in Drake Passage.

These stratification and shear data suggest that the model assumption of a two-layer structure is more appropriate for the south of the Passage than the north and for the austral summer, fall, and spring than winter.

b. Bulk shear statistics and rotary properties

Insight into the range of applicability of the model can be gained by considering the statistics of bulk shear

observed throughout the year from the *LMG*, which show the extent to which it is subject to spiking, and its rotary properties that illustrate the extent to which the near-inertial processes of interest dominate.

The probability distribution functions (PDFs) of bulk shear variance (S^2, Fig. 5) show that it has a non-Gaussian distribution with a distinctly leptokurtic profile (i.e., with a higher peak and fatter tails) in all seasons. This property is confirmed by taking the kurtosis of the distribution (Table 1), where kurtosis values of 12 or greater are found in all seasons (versus a value of three for a Gaussian distribution), which shows that enhancement of shear is an intermittent process with bursts of high shear interspersed among longer intervals of much lower shear, particularly in summer, fall, and spring. The (normalized) standard deviations show that the degree of variation is relatively uniform throughout the year (Table 1).

The highest mean values of bulk S^2 are found in austral summer, fall, and spring (Table 1). The mean values in winter are somewhat lower, despite this being the season of highest wind stress variance in Drake Passage (Thompson et al. 2007). Taken in conjunction with the monthly profiles of S^2 calculated between successive ADCP depth bins in Fig. 4, this could mean the kinetic energy input by the wind, particularly in the north of the Passage, follows a markedly different pathway to dissipation than elsewhere. We return to this point in the
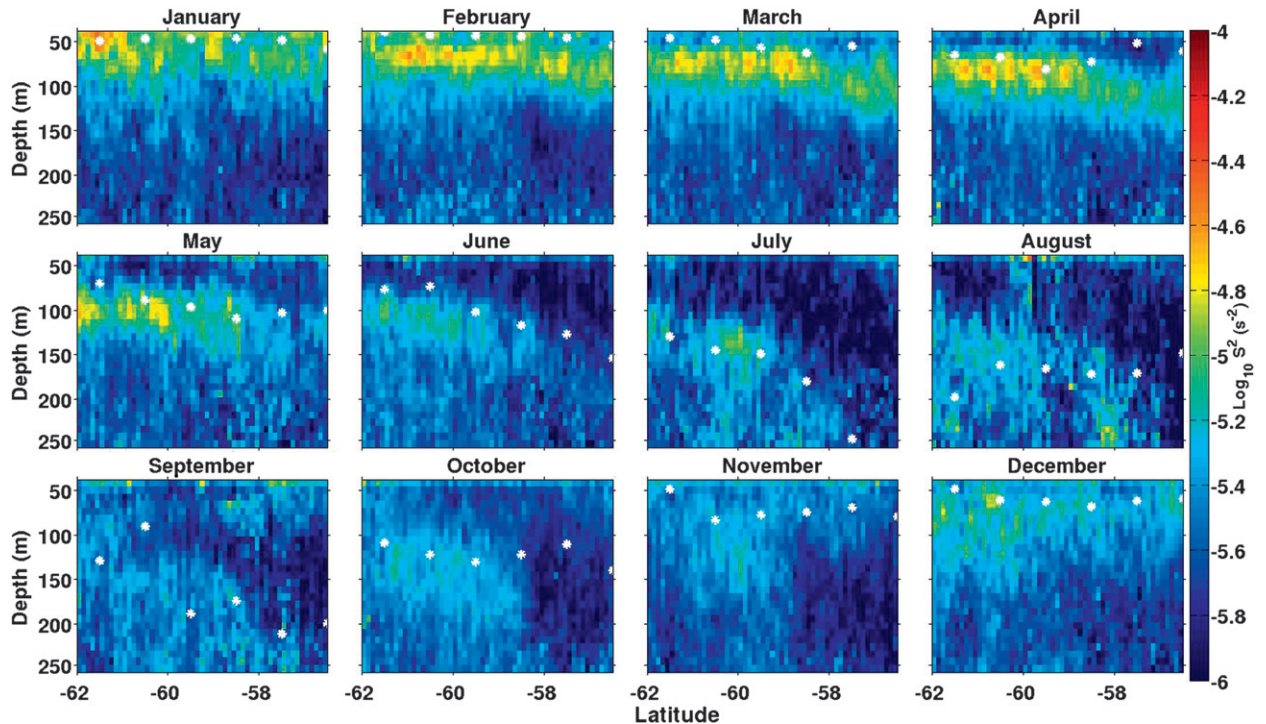
FIG. 4. Estimation of $\log_{10} S^2$ in Drake Passage. Shear has been calculated here as centered differences around ADCP depth bins rather than as a bulk shear. The Dong et al. (2008) mixed layer depth climatology has been marked by white dots to illustrate that high shear usually occurs below the base of the mixed layer. The data show that monthly mean shear tends to be higher and more spatially concentrated in the south of the Passage and in summer.

discussion. Therefore, the two-layer assumption of the model may not be applicable in the regime of the northern Drake Passage.

The inertial frequency in Drake Passage ranges from 0.070 cycles per hour (cph) (14.25-h period) in the north to 0.075 cph (13.25 h) in the south. The rotary spectra of the *Cook* bulk shear peaks at an anticyclonic rotation of 0.072 cph (Fig. 6a), very close to the mean inertial frequency of 0.073 cph. There is much less shear variance rotating cyclonically. The 95% confidence intervals are, however, relatively large owing to the few degrees of freedom in this individual transect, with only the largest peaks significantly different from zero.

The magnitude of the *LMG* bulk shear variance differs between seasons (Fig. 6b) in line with the means shown in Table 1. The spectra in spring and fall have a similar shape with a peak close to the inertial frequency and the variance falls off more slowly at lower frequencies. In summer and winter the peak shear variance occurs at 0.045 cph (22 h), with the remaining variance spread broadly around this (Fig. 6b). On account of the much higher degrees of freedom in this calculation, the shear variance is shown to be significantly different from zero in all seasons at frequencies less than approximately 0.15 cph (6.7 h).

The higher mean, kurtosis, and shear variance at near inertial frequencies of bulk shear in summer, fall, and spring suggest that the model is more applicable in these periods than in winter.

5. Model evaluation

Here, we employ a dual approach to evaluating the proposed open-ocean shear spike generation model with the Drake Passage observations. First, we perform a detailed comparison of $d_t S^2$ (with the subscript denoting differentiation) and predicted shear squared production $P(S^2)$ for the *Cook* transect as set out in (5). Second, we expand our model evaluation over all seasons using the *LMG* data to provide a statistical test of model skill. The dissipation of S^2 by interfacial friction is shown in the appendix to be insignificant with respect to the production of S^2 and is omitted from the comparison.

In the *Cook* transect the model can be evaluated in terms of four distinct regimes found over the transect. The first regime applies to the period from the start of the transect until the start of 10 February (i.e., between 56.8° and 58.1°S) where the weakest S^2 (Fig. 7b), wind stress (Fig. 7a), and stratification (Fig. 2b) during the transect were found. In this interval there were spikes
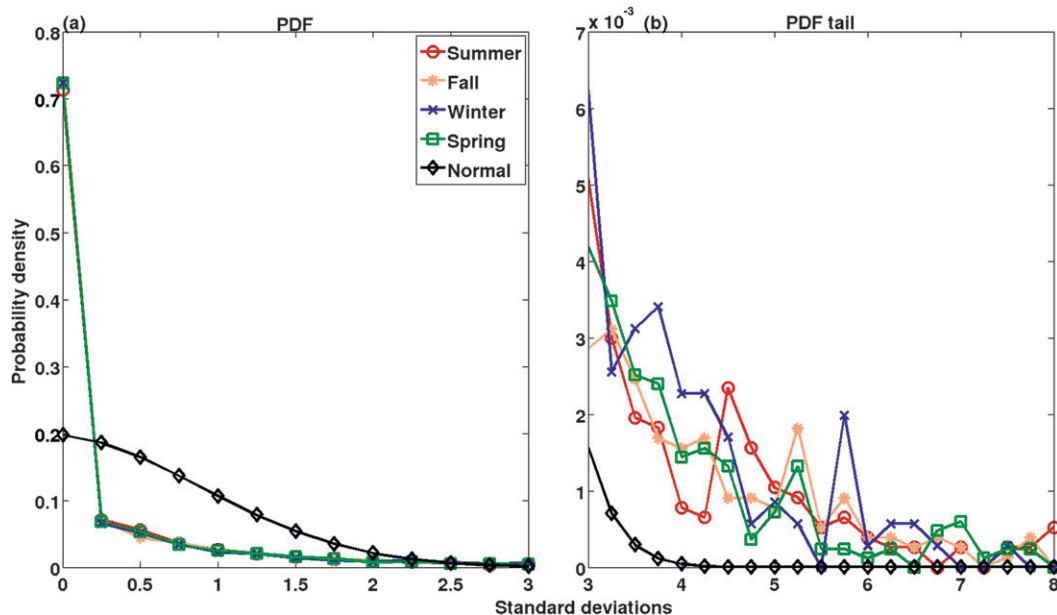
FIG. 5. Probability distribution functions of bulk shear variance in Drake Passage for the *Laurence M. Gould* data where (a) shows the PDFs for standard deviations less than 3 and (b) extends this for the tail of the distribution with a rescaled *y* axis. A Gaussian distribution has been included for comparison. These PDFs have been calculated for each season individually with respect to the standard deviation of that season. The value at each point indicates the proportion of observations within 0.25 standard deviations of that normalized standard deviation.

that coincided with wind shear alignment such as midway through 8 February and early on 9 February (Fig. 7c), though the amplitude of the actual changes was much larger than that predicted by the model. These spikes occurred during periods when the shear vector in Fig. 7d rotated at a near-inertial frequency (i.e., approximately parallel to the black lines in Fig. 7d, which simulate an anticyclonic rotation at the local inertial frequency for comparison purposes). Overall, however, it seems that the model's applicability in this regime of weak stratification and wind stress is low.

The second regime covers the period from the start of 10 February to midway through 11 February (i.e., between 58.1° and 59.1°S). This part of the transect had stronger wind forcing and stratification though the latter was still relatively weak (Fig. 2b). There was again agreement between the model and $d_t S^2$ on the sign of changes in shear variance at near-inertial frequencies over 10 February, though the amplitude of the actual changes remained somewhat larger. Near midday on 11th February, however, a spike in shear variance of similar amplitude was clearly seen in the data and model prediction. This spike was marked by a near-inertial rotation of the shear vector (Fig. 7d) while, in contrast, the wind had almost no rotational component. The model performed better at identifying when near-inertial shear spikes would occur in this regime as the stratification increased.

The third regime was the period of wind stress close to zero (Fig. 7a) from 11 February until later on 12 February (i.e., between 59.1° and 60.6°S). The model obviously predicted low generation of S^2, though this interval was notable for three distinct shear spikes (Fig. 7c), which are unexplained by the model. The wind vector underwent a near reversal in direction in this interval.

The fourth regime spans the interval from 12 February to the end of the transect (i.e., south of 59.1°) when there was once again a strong wind stress. The mixed layer depth varied over this region (Fig. 2b) but was characterized by a sharp transition layer throughout. This interval included a double peak in shear production midway through 13 and early on 14 February (Fig. 7c), which were coincident with wind shear alignment, (Fig. 7d), while the clearest agreement of all between the

TABLE 1. Statistics of bulk shear variance for the *Laurence M. Gould* data where the layer depths have been calculated using the Dong et al. (2008) MLD climatology. The standard deviations have been normalized by the respective mean values.

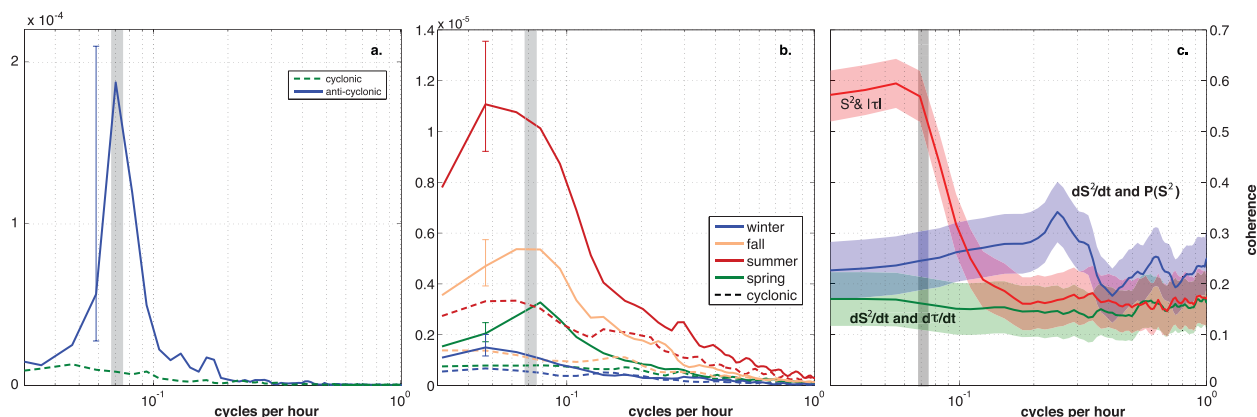| Statistic	Summer	Fall	Winter	Spring
Mean ($10^{-6}\,s^{-2}$)	2.4	1.4	0.5	0.9
Std dev	1.2	1.3	1.3	1.3
Kurtosis	18.1	20.2	12.2	25.2
Number of transects	45	60	40	63

FIG. 6. Rotary spectral analysis of the bulk shear vector in the (a) *Cook* and (b) *Laurence M. Gould* transects averaged by season (s^{-2}); 95% χ^2 confidence intervals are shown. Anticyclonic spectra are plotted as solid lines; cyclonic spectra are plotted as dashed lines. (c) The spectral coherence between S^2 and $|\tau|$ (red), $d_t S^2$ and $P(S^2)$ (blue), $d_t S^2$ and $d_t \tau$ (green) are shown with 95% confidence intervals assuming two degrees of freedom for each of 161 transects of sufficient length included here. Gray shading in (a)–(c) indicates the inertial frequency range of Drake Passage.

observations and model occurred on 15 February, followed by destruction of shear variance which proceeded more rapidly in the observations than predicted by the model. Over this interval of a few hours the near-inertial anticyclonic rotation of the shear vector was less apparent. This was followed by a period in which S^2 fell while wind and shear were opposed. This period of strong

wind stress and stratification is the most applicable for the model.

A challenge to this analysis is determining whether the near-inertial shear arose from inertial oscillations or near-inertial internal waves. This can be better understood by performing a wavelet analysis on the upper and lower layers of one of the velocity components, in this
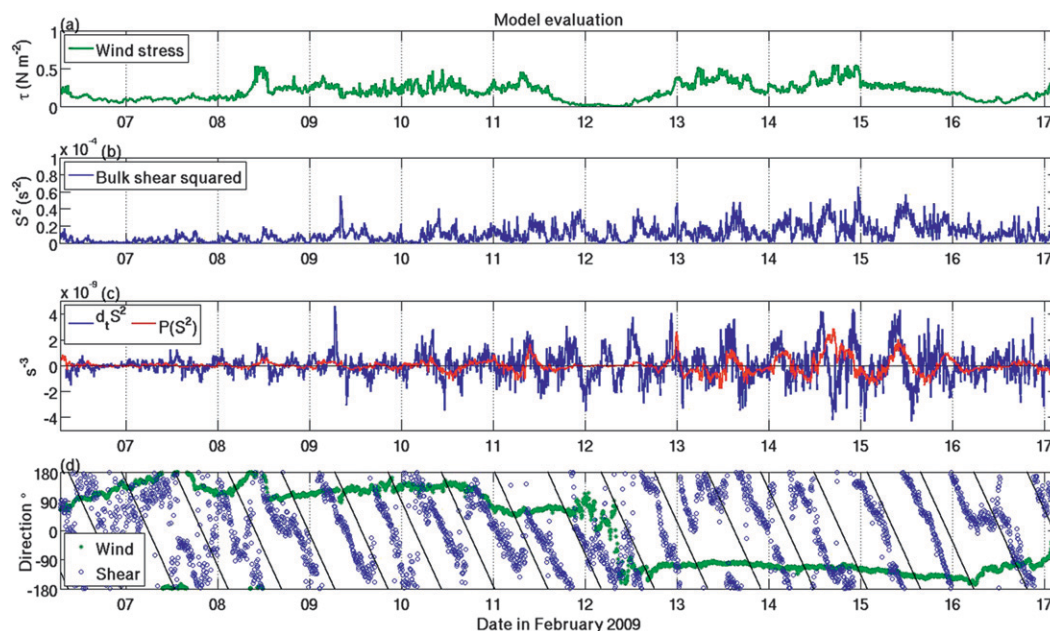

FIG. 7. Observations of the wind and shear along with model output in the *James Cook* transect: (a) magnitude of the wind stress, (b) bulk S^2, (c) a comparison of $d_t S^2$ and $P(S^2)$, and (d) the direction of the wind (green stars) and shear (blue circles) vectors where rotation parallel to the black lines indicates anticyclonic rotation at the local inertial frequency. The direction is calculated relative to due north with rotation positive in a clockwise sense. A 3-h moving average filter has been applied to the $d_t S^2$ time series in (c). All time series are with respect to Universal Time and local time in the region is 4–5 h behind this.
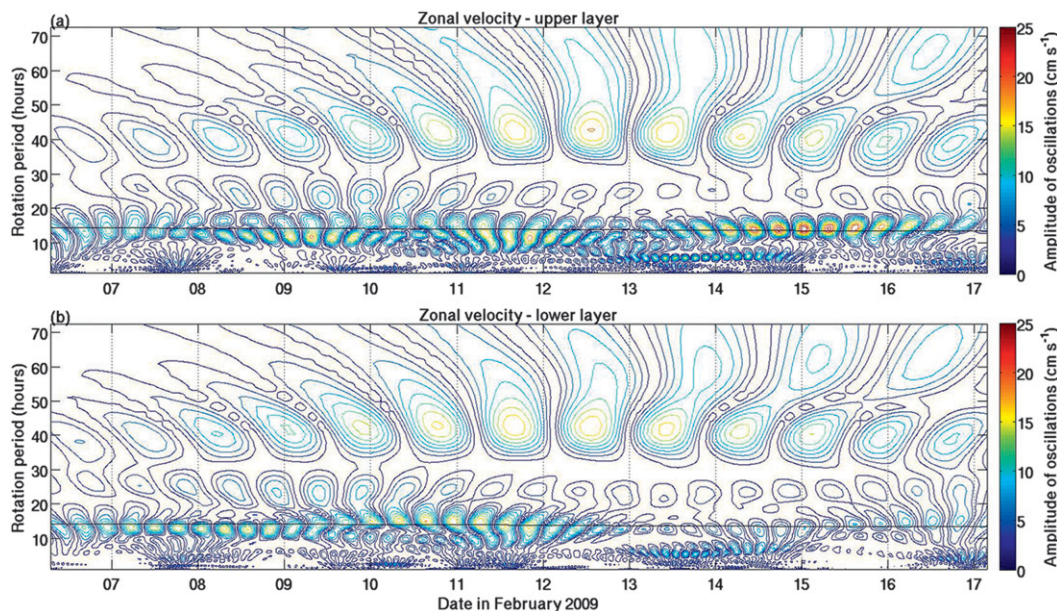
FIG. 8. A wavelet analysis of the zonal velocity in the (a) upper and (b) lower layers used to calculate bulk shear during the *Cook* transect. The colorscale (cm s^{-1}) values correspond to the amplitude of oscillations at each rotational period. The analysis highlights the strong vertical diffusion of velocity variance at the local inertial period (indicated by the horizontal black line) in the north (early in time series) compared to the south of the passage (later in the time series).

case zonal velocity. Figure 8 shows the amplitude of oscillations at different rotational periods (without specifying the sense of the rotation). In the north of the passage (7–12 February in Figs. 8a,b) near-inertial rotation of similar amplitude is apparent in both upper and lower layers (where the local inertial period is indicated by the black line). The structure was quite different in the south of the passage, however, where the rotations were much stronger in the upper layer than in the lower layer. This implies that the near-inertial bulk shear arose in the south of the passage simply by the strong inhibition of vertical momentum fluxes through the transition layer, while the bulk shear arose in the north owing to weak inhibition of vertical momentum fluxes and possibly a more subtle mechanism involving a change in phase of the rotation with depth (Dohan and Davis 2011).

Given the intermittent nature of shear spikes, it is instructive to consider a statistical measure of the model skill using the larger *LMG* dataset (Fig. 6c). We estimated and compared the magnitude-squared coherence (hereafter coherence) between 1) shear-squared and relative surface stress, 2) the time derivatives of the aforementioned, and 3) $d_t S^2$ and predicted $P(S^2)$. All of the estimated coherences differed significantly from zero at 95% confidence. Coherence was highest between the shear-squared and relative surface stress at low

frequencies, suggesting that longer periods of forcing will generate more shear, consistent with previous findings (Grant and Belcher 2011). However, the coherence drops markedly at superinertial frequencies. Notably, the coherence between $d_t S^2$ and predicted $P(S^2)$ exceeded the other estimates with 95% confidence over most of the superinertial frequencies resolved. The peak coherence between $d_t S^2$ and $P(S^2)$ occurs at a higher frequency than the inertial period, reflecting the fact that the key time scale here is the rate of relative rotation of the wind and shear, which is likely to be spread over a range of frequencies owing to the rapid advection of atmospheric features rather than focused on the local inertial frequency.

6. Discussion

A simple two-layer theoretical model for the generation of shear spikes in open ocean conditions has been derived and tested against observations from Drake Passage. The model predicts that shear is generated by the alignment of wind and shear vectors and is destroyed by their opposition, with the destruction of shear by the vertical diffusion of momentum owing to interfacial friction playing a negligible role. In Drake Passage the model's highest skill at predicting shear generation was for near-inertial frequencies when the water column had

a well-defined surface mixed layer above a strongly stratified transition layer. The model was not readily applicable in regions where the surface layer was lightly stratified throughout.

The observed rate of change of S^2 decreased sharply on a number of occasions, in Fig. 7c, in a manner not replicated by the model (e.g., late 14 February and early 15 February). This could reflect processes not represented explicitly in the simple model, such as shear instability which gives rise to turbulent momentum fluxes that operate much more efficiently than those parameterized by the interfacial friction term intended to replicate relatively laminar momentum transfer.

In demonstrating the regimes of applicability of the model, climatologies of stratification and shear variance were presented. The climatologies showed that the south of Drake Passage has higher levels of shear and stratification than the north of the passage throughout the year. It also illustrated that in the north of the passage, shear variance was lower in winter than in summer, despite this being the season of highest wind stress magnitude. These differences may indicate a number of distinct pathways to kinetic energy dissipation in the passage that depend on the location and season of energy input. In the south the presence of sharp stratification may mean more kinetic energy is dissipated in the transition layer if a Kelvin–Helmholtz instability develops or is transferred to the internal wave field if no instability develops. In the north the very weak stratification in winter may mean, instead, that more near-inertial kinetic energy is projected onto the barotropic or low vertical wavenumber baroclinic modes, though this would decrease as the stratification becomes stronger in summer. A separate study would be required to confirm this.

A notable feature of Fig. 7d is the tendency for the shear vector rotation to be coherent in phase over long intervals. From late on 13 February to the first half of 16 February, for example, the shear vector had a clear near-inertial rotation that was coherent in phase over an interval in which the ship covered a distance of about 180 km. Although the existence of inertial rotations over such a range is a simple consequence of the length scale of atmospheric motions, the significant phase coherence of this rotation along the track may imply that the shear spiking events analyzed here are of substantial horizontal extent.

The main motivation for investigating shear spikes is as a possible trigger for the development of shear instabilities and thus diapycnal mixing. Although the spatial and temporal resolution of these datasets is too coarse to estimate this directly, the intermittency of shear production predicted by the model is consistent with estimates of dissipation of turbulent kinetic energy made with microstructure instruments (e.g., Gregg et al. 1993). Furthermore, these spikes in shear occurred without a wind stress rotating at the local inertial frequency and so may be more widely prevalent than the resonant case. The shear spiking model does reduce to a continuous production of S^2 in the special case of a resonant wind. The shear spiking mechanism could have important local effects in mixing the water column, as it could repeatedly provide nutrient fluxes from the interior into the light-rich surface layer over a summer stratified period in the open ocean (Parslow et al. 2001) sustaining a deep chlorophyll maximum.

APPENDIX

Role of Interfacial Friction in Shear Generation

We investigated the role of interfacial friction in the shear generation process. Again following BR09, the interfacial drag term can be parameterized as follows:

$$c_i h_s^2 S^2 = \kappa S_{\text{if}}, \quad\quad\quad (A1)$$

where κ is the interfacial eddy viscosity and S_{if} is the interfacial shear. With $S_{\text{if}} = 5 \times 10^{-3}\,\text{s}^{-1}(\pm 4 \times 10^{-5}\,\text{s}^{-1})$ taken as the mean of shear between successive ADCP depth bins in the high shear layer during the *Cook* cruise, $h_s = 40\,\text{m}$, and an assumption of $\kappa = 10^{-5}\,\text{m}^2\,\text{s}^{-1}$ as a typical ocean interior eddy viscosity value (Moum and Rippeth 2009) to within an order of magnitude. This

gives a nondimensional interfacial drag coefficient of 10^{-4}. Furthermore, if we assume the following scale values (again based on observations from the *Cook* cruise): $S = 10^{-3}\,\mathrm{s}^{-1}$, $T_w = 10^{-1}\,\mathrm{N\,m}^{-2}$, $T = 10^2\,\mathrm{s}$, $h_s = 40\,\mathrm{m}$, and $H = 100\,\mathrm{m}$, then the shear production term $P(S^2)$ is $O(10^{-8})$ while the dissipation term $D(S^2)$ is $O(10^{-14})$. This scale analysis leads to the conclusion that the interfacial friction term can be neglected in the evaluation of the model.

REFERENCES

Burchard, H., and T. Rippeth, 2009: Generation of bulk shear spikes in shallow stratified tidal seas. *J. Phys. Oceanogr.,* **39,** 969–985.

D'Asaro, E., 1985: The energy flux from the wind to near-inertial motions in the surface mixed layer. *J. Phys. Oceanogr.,* **14,** 1043–1059.

Dohan, K., and R. Davis, 2011: Mixing in the transition layer during two storm events. *J. Phys. Oceanogr.,* **41,** 42–66.

Dong, S., J. Sprintall, S. Gille, and L. Talley, 2008: Southern Ocean mixed-layer depth from Argo float profiles. *J. Geophys. Res.,* **113,** C06013, doi:10.1029/2006JC004051.

Firing, E., J. Hummon, and T. Chereskin, 2012: Improving the quality and accessibility of current profile measurements in the Southern Ocean. *Oceanography (Washington D.C.),* **25,** 164–165.

Firing, Y., T. Chereskin, and M. Mazloff, 2011: Vertical structure and transport of the Antarctic Circumpolar Current in Drake Passage from direct velocity observations. *J. Geophys. Res.,* **116,** C08015, doi:10.1029/2011JC006999.

Gille, S., 2005: Statistical characterization of zonal and meridional ocean wind stress. *J. Atmos. Oceanic Technol.,* **22,** 1353–1372.

Grant, A., and S. Belcher, 2011: Wind-driven mixing below the oceanic mixed layer. *J. Phys. Oceanogr.,* **41,** 1556–1575.

Gregg, M., H. Seim, and D. Percival, 1993: Statistics of shear and turbulent dissipation profiles in random internal wave fields. *J. Phys. Oceanogr.,* **23,** 1777–1799.

Hamersley, D., and E. McDonagh, Eds., 2009: RRS James Cook Cruise JC031, 03 Feb–03 Mar 2009. Hydrographic sections of Drake Passage. National Oceanography Centre Cruise Rep. 39, 170 pp. [Available online at http://eprints.soton.ac.uk/69897/.]

Johnston, T., and D. Rudnick, 2009: Observations of the transition layer. *J. Phys. Oceanogr.,* **39,** 780–797.

Large, W., and S. Pond, 1981: Open ocean momentum flux measurements in moderate to strong winds. *J. Phys. Oceanogr.,* **11,** 324–336.

Lenn, Y.-D., T. Chereskin, J. Sprintall, and E. Firing, 2007: Mean jets, mesoscale variability and eddy momentum fluxes in the surface layer of the Antarctic Circumpolar Current in Drake Passage. *J. Mar. Res.,* **65,** 27–58.

——, T. Rippeth, C. Old, S. Bacon, I. Polyakov, V. Ivanov, and J. Hoelemann, 2011: Intermittent intense turbulent mixing under ice in the Laptev Sea continental shelf. *J. Phys. Oceanogr.,* **41,** 531–547.

Mahadevan, A., E. D'Asaro, M.-J. Perry, and C. Lee, 2012: Eddy-driven stratification initiates North Atlantic Spring phytoplankton blooms. *Science,* **337,** 54–58.

Marshall, D., and H. Pillar, 2011: Momentum balance of the wind-driven and meridional overturning circulation. *J. Phys. Oceanogr.,* **41,** 960–978.

Moum, J., and T. Rippeth, 2009: Do observations adequately resolve the natural variability of oceanic turbulence? *J. Mar. Syst.,* **77,** 409–417.

Parslow, J., P. Boyd, S. Rintoul, and F. Griffiths, 2001: A persistent subsurface chlorophyll maximum in the Interpolar Frontal Zone south of Australia: Seasonal progression and implications for phytoplankton–light–nutrient interactions. *J. Geophys. Res.,* **106** (C12), 31 543–31 557.

Plueddemann, A., and J. Farrar, 2006: Observations and models of the energy flux from the wind to mixed-layer inertial currents. *Deep-Sea Res. II,* **53,** 5–30.

Pollard, R., and R. Millard, 1970: Comparison between observed and simulated wind-generated inertial oscillations. *Deep-Sea Res.,* **17,** 813–821.

Polton, J., J. Smith, J. MacKinnon, and A. Tejada-Martinez, 2008: Rapid generation of high-frequency internal waves beneath a wind and wave forced oceanic surface mixed layer. *Geophys. Res. Lett.,* **35,** L13602, doi:10.1029/2008GL033856.

Rippeth, T., P. Wiles, M. Palmer, J. Sharples, and J. Tweddle, 2009: The diapycnal nutrient flux and shear-induced diapycnal mixing in the seasonally stratified western Irish Sea. *Cont. Shelf Res.,* **29,** 1580–1587.

Roemmich, D., 1983: Optimal estimation of hydrographic station data and derived fields. *J. Phys. Oceanogr.,* **13,** 1544–1549.

Skyllingstad, E., W. Smyth, and G. Crawford, 1998: Resonant wind-driven mixing in the ocean boundary layer. *J. Phys. Oceanogr.,* **30,** 1866–1890.

Sprintall, J., 2003: Seasonal to interannual upper-ocean variability in the Drake Passage. *J. Mar. Res.,* **61,** 27–57.

Sullivan, P., and J. McWilliams, 2010: Dynamics of winds and currents coupled to surface waves. *Annu. Rev. Fluid Mech.,* **42,** 19–42.

Thompson, A., S. Gille, J. MacKinnon, and J. Sprintall, 2007: Spatial and temporal patterns of small-scale mixing in Drake Passage. *J. Phys. Oceanogr.,* **37,** 572–592.

Thorpe, S., 2004: Langmuir circulation. *Annu. Rev. Fluid Mech.,* **36,** 55–79.